The International Journal of Advanced Manufacturing Technology (2018) 99:707–727
https://doi.org/10.1007/s00170-018-2466-z

ORIGINAL ARTICLE

Dressing strategy and grinding control for cylindrical microstructural surface

Haoyang Cao [1] · Xun Chen [2] · Haolin Li [1]

Received: 25 January 2018 / Accepted: 17 July 2018 / Published online: 9 August 2018

Abstract

Surface structural texture is designed to achieve specific functional performance for many advanced applications. After a brief review of current manufacturing methods for textural surface, this paper focuses on the study of microstructural surface creation by grinding. The axial and peripheral cross-sections of textured wheels under different dressing overlap ratios U_d are illustrated. A set of microstructural texturing models are proposed and the influences of dressing and grinding parameters are discussed. The texture formation is analysed in considering each cutting point in grinding kinematic movement. A significant effect of the grinding contact length on the texture formation is noticed, which defines a texture pattern limitation for grinding to manipulate. Typical surface texture characteristics are introduced to assess the structural surface features and the corresponding theoretical models are validated by experimental results. The relationships between the textural gouge size and the kinematic conditions of dressing and grinding have been delineated for the guidance of grinding texturing strategy. The component waviness on textured components clearly shows the importance of rotational ratio on the layout of microstructural texture. The paper lays down an important foundation for surface microstructural texturing by grinding.

Keywords Microstructural surface · Grinding kinematics · Dressing · Modelling · Surface assessment

Nomenclature

a_p	Grinding depth (μm)
b	The length of undressed wheel surface in axial cross-section (μm)
b_d	Dressing tool engagement width (μm)
b_w	Gouge width (μm)
f_d	Pitch of helical groove (dressing feed) (μm)
f_{uc}	Uncut ratio
a_d	Height of a helical groove (dressing depth) (μm)
h_s	Nominal peak to valley height (μm)
K_1, K_2	Angles between the tangents to a helical groove profile and wheel surface
l_k	Grinding kinematic contact length (μm)
l_w	Gouge length (μm)
l_{wk}	Gouge length in kinematic model (μm)
L	Longitudinal pitch of grooves on work material (μm)
n	Number of grain vertices at wheel circumference
n_w	Workpiece rotational speed (rpm)
n_s	Grinding wheel rotational speed (rpm)
$p = n_s/n_w$	Rotational speed ratio between workpiece and wheel
$q = v_w/v_s$	Speed ratio between work speed and wheel speed
r	Radius of the imagined wheel, rolling without slip along rolling line (mm)
R_s	Grinding wheel radius (mm)
R_e	The equivalent radius of grinding wheel (mm), $R_e = R_s R_w / (R_s + R_w)$
R_w	Workpiece radius (mm)
r_d	Radius of diamond dresser tip (mm)
U_d	Dressing ratio, $U_d = b_d / f_d$
v_s	Grinding speed (ms^{-1})
v_w	Work material speed (ms^{-1})
l_x	Uncut length of the workpiece
x_{en}	Point where grain enters into work material
x_{ex}	Point where grain exits from work material
$\Delta\alpha$	Angle between adjacent grain vertices in the polar system

✉ Xun Chen
x.chen@ljmu.ac.uk

[1] College of Mechanical Engineering, University of Shanghai for Science and Technology, Shanghai 200093, China

[2] Advanced Manufacturing Technology Research Laboratory, General Engineering Research Institute, Liverpool John Moores University, Liverpool L3 3AF, UK

α	Angular coordinate of cutting edges in polar system (rad)
$\rho(\alpha)$	Radius of nominal profile of grinding wheel (mm)
φ	Angle of wheel rotation (rad)
φ_{en}	The angle grain enter into work-material
φ_{ex}	The angle grain exit from work-material

1 Introduction

A structured surface plays a decisive role in the functional performance of engineering parts. Over the last few decades, many interesting investigations have been conducted to understand the influence of structured surface texture, particularly at a micrometre and nanometre scale, on engineered surface performance in many advanced application fields [1]. A structured surface may be considered as "patterned" surface with some regular array of surface features amenable to some sensible deterministic description. However, such surfaces have a deterministic pattern of defined aspect ratio and obvious commonality with other structured surfaces in terms of manufacture and metrology [2]. In a CIRP meeting in 1998, Stout [3] gave a revised classification for some manufactured surfaces:

> 'Structured surfaces' are those where the surface structure is a design feature intended to give specific functional performance [3].

1.1 Beneficial functions of textured surface

Compared to conventional smooth surfaces, textured surfaces show many advantageous property functions. Some concepts of texture find their inspiration in nature. Many biological examples of textured surfaces can be found which are not yet completely understood, but these surface textures have been successfully used in many applications to improve the performance of surfaces, especially in surface drag or friction reduction.

The typical structure of drag reduction is sharkskin, which possesses many small regular grooves on the surface of scales. These grooves inhibit the turbulence and reduce drag resistance. Because of such advantage of the microstructure, many kinds of simplified straight microgrooves imitating sharkskin have been manufactured with a certain level of satisfactory performance [4, 5]. By using 25.4- and 50.8-mm-diameter pipes lined with a film of microgrooved equilateral triangles of base 0.11 mm, Liu et al. [6] demonstrated the drag-reducing efficiency could reach 5–7% in fully developed turbulent water flow. With biomimetic technology study, Luo and Zhang [7] applied microgrooved surface in nature gas pipelining to reduce drag and showed that the pressure loss can be decreased more than 8% at the same circumstance in field. In order to reduce drag in turbulent flow, Denkena [8] ground special designed riblet surface (microgrooves with a width of 40 μm and depth of 20 μm) on the surfaces of compressor blades and achieved 2.7~4% maximum shear stress reduction.

Another potential successful application of textured surface in engineering is the improvement of tribological performance in friction reduction. Microstructure, such as small pockets, cavities, and grooves, can perform the functions of a hydrostatic microbearing. When two mating surfaces approach each other, the fluid in the cavities is compressed producing a bearing pressure. Once a surface possesses a microstructural pattern, it can change contact pressure distribution, surface fluid hydrodynamic behaviour, and surfaces' deformation considerably, leading to different surface lubrication performances [1, 9, 10].

Andersson et al. [10] investigated the beneficial effects of laser-textured surfaces on tool friction reduction. They carried out a set of wear tests for laser-textured surfaces under lubricated sliding conditions in comparison to smooth surfaces. Each test was stopped when the coefficient of friction reached the value $\mu = 0.2$ without considering the initial value of friction coefficient. The number of maximum sliding cycles for textured surface was over 1000, while for the smooth surface was only 11. Dumitru et al. [11] reported their investigation of the effect of surface textures using tribological tests on laser-textured structure substrates and showed that the lifetime of laser processed structural texture samples is eight times longer than the value of untextured samples. With pin-on-disk tests of silicon nitride ceramic mated with hardened steel, Wakuda et al. [12] verified the surface microtexture is an effective key to friction reduction. Compared to a lapped smooth surface, some textured samples successfully realised friction coefficient reductions from 0.12 to 0.10. Under unidirectional pin-on-disk configuration, Ramesh et al. [13] reported their analysis results, in which the surfaces with micrometre-scale textures exhibit lower friction as much as 80% of untextured surfaces under hydrodynamic lubrication. In their study, the microstructure surface textures of dimple size 28~257 μm offered the benefit of reducing drug and friction in both lubrication and hydrodynamic regimes, decreasing wear and providing extra load support.

1.2 Texturing methods

Many techniques are currently available to create structure surface with sizes in the micrometre range. Diamond turning processes generate structural surface by rotating the workpiece copying the geometry of the diamond tool into the surface. The shape of microstructure is determined either by the geometry of the diamond tool (profile turning) or by the modulation of the infeed depth (form turning). Structure that is more complex can be generated by controlling both linear axes, but it is limited to rotationally symmetric structure surfaces [14, 15]. Unlike diamond turning operations which use a stationary cutting tool that

is fed past a rotating workpiece, fly-cutting is a milling process using one single diamond tool that is revolving on an aerostatic supported high-precision spindle. By machining grooves in different intersecting directions with different tool geometries, a great variety of complex microstructure can be created. The associated problem with such a method is long time-consuming and the G-code generation [16–18].

Laser surface texture (LST) has demonstrated impressive results in many reported researches [10, 19, 20]. The type of interaction between the laser beam and the material being ablated depends not only on the thermo-optical properties of the workpiece for a given laser (wavelength) irradiation, but also the appropriate choice of the laser processing parameters. Despite the fact that laser processing the surface can effectively produce some complex structures on a component surface, its drawbacks are evident including material melting, burr formation, size inconsistent, and low production rate [10, 19, 20].

Normally, grinding is a precision machining method for a component finishing process that produces smooth surface with tight tolerance and low surface roughness. Grinding with a pattern-dressed wheel to manufacturing microstructural surface texture could be a simple, repeatable, and inexpensive method, which allows different types of patterns on the flat and cylindrical surfaces while maintains the high surface quantity. In order to reduce the influence of the wheel topography stochastic variation in grinding, significant efforts have been made to investigate the texturing/patterning methods for conventional grinding wheels, so that wheel-workpiece contacts can be stabilised. Consequently, grinding becomes a less stochastically dependent process. Li and Axinte [21] presented an informative literature survey of research and development in relation to textured grinding wheels and their advanced future engineering applications.

E. Brinksmeier et al. [22] demonstrated that ultra-precision grinding is employed as an intermediate or pre-finish machining step in the production. Many researches have explored the potential application of microstructural by grinding. Aurich et al. [23] presented an efficient microgrinding tool with cylindrical tool tip diameter between 13 and 100 μm to manufacture complex structured surface. Microstructured surfaces in optical quality are generated by using these microgrinding tools; meanwhile, the structured surface is suitable for many optical moulds and dies. However, the process is only suitable for relative small features due to its slow speed (1 mm/min). Xie et al. [24] presented a fabrication method of micropyramid-structured silicon surface with top radius of 48.3 μm by using crossed grooving with a 60° V-tip of diamond grinding wheel. Because of the limitation of wheel shape, each grinding pass can only create one texture element, and it still needs a long time to texture the whole surface. The micropyramid-structured of grinding surface can significantly improve cooling performances at the same wall superheat. Yutaka et al. [25] combined angle fine particle peening (FPP) and precision surface grinding to fabricate microtextured surfaces with valleys, dimples, and plateaus. Surface grinding successfully removed the ridge peaks, resulting in the average ridge height in 10 μm and the average ridge pitch in 200 μm. Because the surface texture is created by peening process, the feature is not easy controlled in a defined way.

Considering the grinding wheel surface can be controlled by dressing operation, many structural surfaces could be created quickly and cheaply by controlling proper dressing and grinding processes. Bottene et al. [26] discussed technologies for surface functionalization and presented a new method to produce tailored surfaces via grinding process. They have demonstrated a good potential for various texture creations by dressing and grinding. However, the kinematics of such a microtexturing method has not been discussed in detail.

Stepien has first demonstrated the method for a single-point dresser to create a patterned structural surface in 1989 [27]. By dressing helical grooves twice on a wheel nominal surface, the grooves shaped on the workpiece are the result of the reproduction of wheel surface pattern. When the profile of dresser tip is presented by the function of its axial cross-section, Stepien developed two models (deterministic and probabilistic) of the wheel surface and kinematical path equations of grains under the condition of dressing overlap ratio $U_d < 1$, assuming different grain arrangements after dressing in the wheel circumference. The models show the speed ratio between wheel and workpiece during the texture generation is an important factor. The patterned texture of the workpiece measured shows high accord with the pattern simulation results base on the models [28–30]. However, most Stepien's research and experiments are of macroscale (few millimetre level) texture on the flat surface grinding. With the potential functional benefits of microstructural surface, it is important to investigate applicable grinding method that could generate structural profile at micrometre level, where the dressing overlap ratio is often larger than 1.

Oliveira et al. [31, 32] connected an electro-mechanical exciter to a dressing roller with synchronised signal from a control software to engrave patterns on a grinding wheel. The method is based on the introduction of a controlled external excitation in the dressing tool to dynamically change the dressing depth (a_d) during the dressing operation, which allows the patterns to be produced in every wheel rotation. The production of textured workpiece is realised by using the patterned grinding wheel and integer angular speed ratio between workpiece and wheel during grinding. Moreover, the qualities of dressing and grinding operations were evaluated using the AE mapping technique. The map representing the AE distribution around the grinding wheel along the time axis can be used for process monitoring and control. With such a method, they create a texture of square-shaped pockets with side of 1.5 mm. Silva et al. [33] further used the same dressing system and AE mapping technique to produce profiled workpiece surface patterns. The dressing tool they used was a square-shaped single-point diamond of section size 0.6 mm × 0.6 mm.

Denkana et al. [8, 34] introduced a microprofile dressing and grinding process for the creation of riblet surface that can reduce

the near wall turbulent friction. For the generation of microprofile on grinding wheel, form-dressing operation using a form roller was investigated. The wheel profile geometry has been generated by applying a profile dressing process with a profile kinematic shift. In the first plunge motion, one flank of the profiles is dressed. The second plunge motion is carried out with an axial offset of the dressing roller, whereby the other flank of the profiles is dressed. Afterward, the grinding strategies with profile overlapping have been developed to create continuous riblets with the required small distances. At first, single profiles are ground onto the workpiece. In the second step, the defined profile is ground with an axial profile offset. The desired riblet profiles could be created by repeatedly offsetting the single profile. In their investigation, a set of riblet structures with a width between 20 and 120 μm are obtained with a profile aspect ratio of 0.5.

As aforementioned, most grinding texturing methods investigated focus on macrotexturing structures featured at millimetre level. But the scaling effects have influence on the surface friction function. Deep drawing experiments and theoretical analysis by Vollertsen et al. [35] prove that the friction coefficients prevailing at the different tribologically active areas are varying over geometry; meanwhile, the size effect also affects the tribology. The other tribological results also show that good friction performance is reached in the textures of size 100~200 μm on stainless steel surfaces [13]. Braun et al. [36] also tested the tribological behaviour of steel sliding pairs with dimples ranging from 15 to 800 μm in diameter. The dimple diameter resulting in the highest friction reduction is in the range of 40 to 200 μm. According to these findings, the tribological beneficial textures are of the feature size less than a millimetre level. Therefore, the focus of grinding surface texturing should move from macro- to microdomain for friction reduction. In this paper, an investigation on the creation of microstructure (sub-millimetre level) with cylindrical plunge grinding operation is presented. A suitable dressing and grinding control strategy is established based on detailed theoretical analysis. The relationships between the textural features of microstructural surface and the operational conditions of dressing and grinding have been analysed in relation to grinding wheel surface geometrical patterns. Further investigation of grinding kinematics at the abrasive grit is provided to illustrate the surface texture creation. The experimental validation is presented to provide a comparison with the theoretical analysis. Based on the positive results, some useful guidelines are drawn to support dressing and grinding operation for surface texture grinding.

2 Microstructural surface texture creation by grinding

The formation mechanism of grinding wheel nominal surface structural pattern is described with the deterministic method. For simplification, assuming the grinding wheel is filled abrasive grains, fully ignoring the grain shape. By considering dressing, grinding parameters, and the kinematic movement of grains, the workpiece topography in axial and circumference direction can be determined. The grinding wheel is dressed with a dresser that passes from right to left and from left to right, which creates a net pattern on the wheel surface. During grinding, the grinding wheel will print its net pattern on the ground workpiece surface forming the surface texture. With properly selected dressing and grinding parameters, where grinding depth a_p is smaller than the dressing depth a_d, different dimple textures can be created on the workpiece surface. A schematic view of the surfaces of the wheels and workpiece is shown in Fig. 1.

2.1 Dressing strategy for wheel surface pattern creation

The grinding wheel topography is simply determined by the characteristics of the wheel and dressing tool together with the relative motion between the dresser and the wheel. The dresser moves across the wheel surface with a dressing lead f_d per wheel revolution while removing wheel surface with a dressing depth a_d. There will be many helical grooves generated in the grinding wheel when using a multiple-point diamond dressing tool.

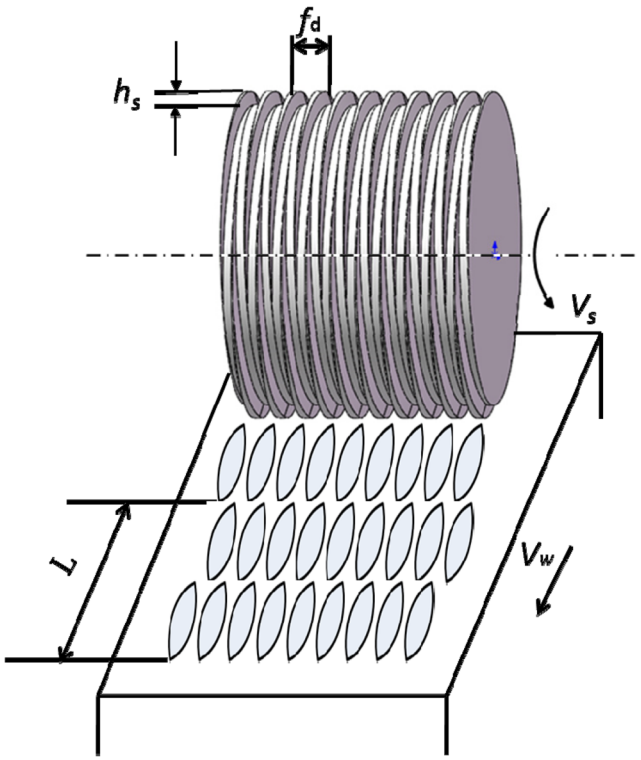

Fig. 1 Schematic views of grinding with the pattern wheels for shaping texture on cylinder surfaces

In order to obtain a grid pattern on the wheel, the strategy of dressing is that the grinding wheel needs to be dressed in a reciprocating manner. Such a dressing method can make two sets of grooves across each other to form the grid pattern on the wheel. When the patterned wheel is used for cylindrical grinding, the top of workpiece surface will be ground off and the wheel pattern will be transferred to the workpiece. The patterned wheel surface reflects the features of dressing path that is determined by dressing parameters and dresser apex radius.

The material removal mechanism in dressing involves bond fracture and abrasive grain break-off caused by crushing actions of the diamond dresser on the wheel. Therefore, the dressing contour cannot be the same as the dressing tool profile [36]. Meanwhile, dressing interaction will make the dresser worn causing its profile change [37]. However, compared to the fracture of abrasive grains, it is reasonable to assume the dresser wear in a dressing operation is so small that it can be ignored. Under such an assumption, the wheel model during dressing and the generation of structural geometry and texture model is more stable and repeatable.

When dressing with a single diamond dresser, the engagement between the dresser and the grinding wheel depends on the dresser shape, abrasive grit shape, and distribution as well as on the dressing parameters. The most important parameters are the dressing feed f_d, the dressing overlap ratio U_d, and the dressing depth of cut a_d. The dressing overlap ratio U_d is the quotient of the engagement width b_d to the dressing feed f_d and shows how often a point on the wheel peripheral face is engaged by the dressing tool.

$$U_d = b_d / f_d \tag{1}$$

When the overlap ratio is $U_d = 1$, with which each peripheral point of the wheel is engaged only once by the dressing tool. Under the situation of $U_d > 1$, dressing results in a finer wheel topography; contrarily, $U_d < 1$ means a part of grinding wheel surface will not be dressed. Moreover, dressing feed rate f_d affects the interval and density of the structure surface texture in the workpiece. If the dressing feed is smaller, the dress cutting number will increase per unit area.

The model of along wheel dressing axial and peripheral cross-section profiles can be divided into two groups according to overlap ratio U_d value ($U_d < 1$ and $U_d \geq 1$). Figure 2 shows a wheel surface profile with dressing overlap ratio $U_d < 1$, where a part of wheel surface is not dressed. The undressed part of the wheel is of the largest radius, which is defined as the equivalent wheel radius R_e in grinding. R_s and R_w are grinding wheel radius and workpiece radius respectively.

$$R_e = \frac{R_s R_w}{R_s + R_w} \tag{2}$$

The profile of dressed grinding wheel illustrated in Fig. 2a can be depicted by helical groove of depth that corresponds to a_d, dressing lead f_d, the length of undressed wheel surface b, and angles K_1 and K_2 between the tangents to a helical groove profile and the wheel nominal surface. As shown in Fig. 2b, a simple conversion $z = \frac{f_d}{2\pi}\alpha$ allows wheel peripheral profile in a cross-section to be determined by radius $\rho(\alpha)$ in the range of $0 \leq \alpha \leq 2\pi$, according to Eq. 3.

$$\begin{cases} \rho(\alpha) = R_e & 0 \leq \alpha \leq \alpha_1 \\ \rho(\alpha) = R_e - f\left(\frac{f_d}{2\pi}\alpha\right) & \alpha_1 \leq \alpha \leq \alpha_2 \end{cases} \tag{3}$$

When grinding depth of cut a_p is given, points C and E limit the fragment of potential inactive wheel circumference. Assuming diamond dresser apex is of spherical radius r_d, the local wheel radius can be calculated as:

$$\begin{cases} \rho(\alpha) = R_e & \text{for} \quad 0 \leq \alpha \leq \alpha_1 \\ \rho(\alpha) = R_e + r_d - a_d - \sqrt{r_d^2 - \left(f_d \frac{\alpha}{2\pi} - \frac{f_d + b}{2}\right)^2} & \text{for} \quad \alpha_1 \leq \alpha \leq 2\pi \end{cases} \tag{4}$$

Combined with the grinding parameters, the variation of grinding wheel radius will reproduce a pattern on the workpiece surface. As shown in Fig. 2, wheel surface between 0 and α_1 is not dressed. If the grinding depth of cut is a_p, the wheel surface between α_2 and α_3 will not cut the workpiece; other grinding wheel parts will engage with the workpiece and remove the materials. The values of α_1, α_2, and α_3 can be determined by Eqs. 5 to 7. The wheel surface between α_3 to 2π and α_1 to α_2 is cut-in phase and cut-out phase with the workpiece respectively. Equations 4~7 reflect the characteristic of wheel profile in Fig. 2, which defines the shape of the wheel profile.

$$\alpha_1 = 2\pi\left(1 - \frac{2\sqrt{a_d(2r_d - a_d)}}{f_d}\right) \tag{5}$$

$$\alpha_2 = 2\pi\left(1 - \frac{\sqrt{a_d(2r_d - a_d)}}{f_d} - \frac{\sqrt{(a_d - a_p)(2r_d - a_d + a_p)}}{f_d}\right) \tag{6}$$

$$\alpha_3 = 2\pi\left(1 - \frac{\sqrt{a_d(2r_d - a_d)}}{f_d} + \frac{\sqrt{(a_d - a_p)(2r_d - a_d + a_p)}}{f_d}\right) \tag{7}$$

When the dresser tip is in spherical shape, the angles K_1 and K_2 are determined by:

$$K_1 = K_2 = \arctan\sqrt{\frac{2a_d}{r_d - a_d}} \tag{8}$$

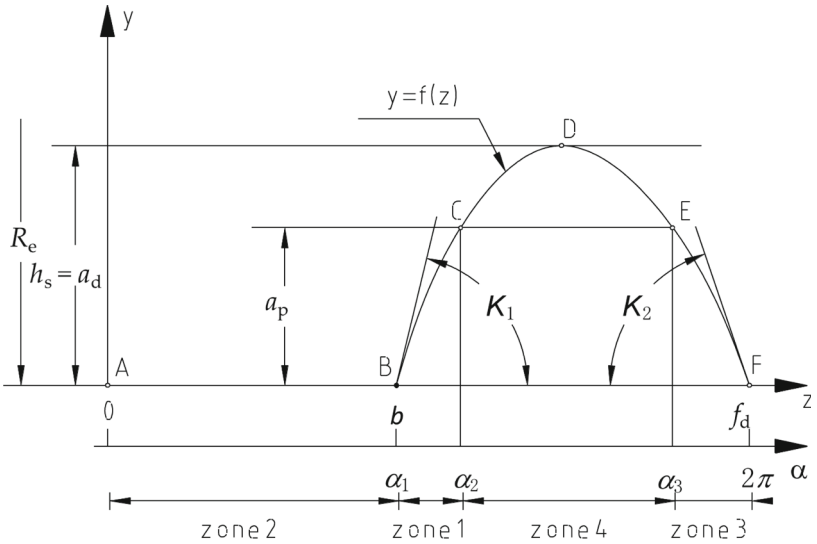

(a) Axial cross section profile of dressed wheel (U_d <1, i.e. $b_d < f_d$)

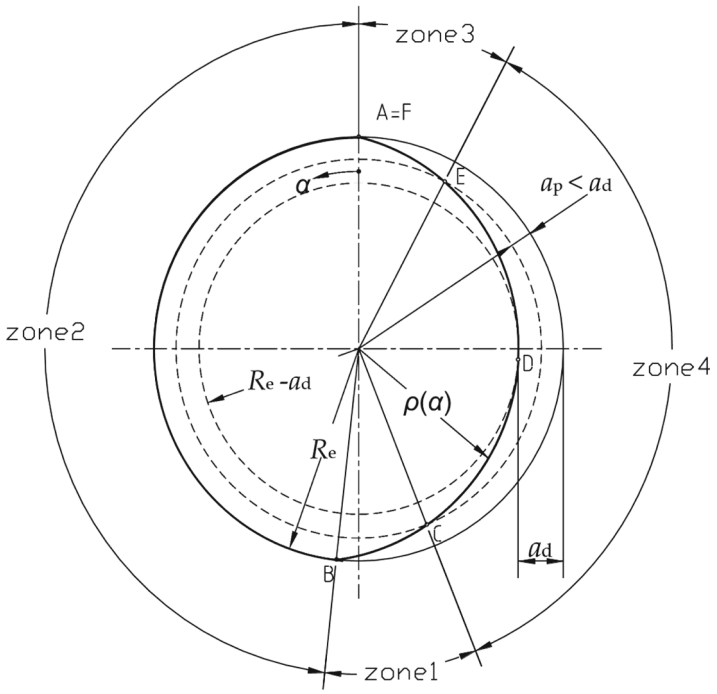

(b) peripheral cross section profile of dressed wheel (U_d <1, i.e. $b_d < f_d$)

Fig. 2 Generalised dressed wheel profile when $U_d < 1$. **a** Axial cross-section profile of dressed wheel ($U_d < 1$, i.e. $b_d < f_d$). **b** Peripheral cross-section profile of dressed wheel ($U_d < 1$, i.e. $b_d < f_d$)

Other feature parameters of dressed wheel profile shown in Fig. 2 (for $U_d < 1$) include:

- The deepest depth of dressed grove is at the position D, which equals a_d
- AF = f_d, is dressing lead
- BF = $2\sqrt{a_d(2r_d - a_d)} = b_d$, which is regard as the dressing tool engagement width
- AB = $b = f_d - b_d$

Substitute these values into Eq. 4, the wheel surface profile model becomes

$$\begin{cases} \rho(\alpha) = R_e & \text{for} \quad 0 \le \alpha \le \alpha_1 \\ \rho(\alpha) = R_e + r_d - a_d - \sqrt{r_d^2 - \left(f_d \frac{\alpha}{2\pi} - f_d + \frac{b_d}{2}\right)^2} & \text{for} \quad \alpha_1 \le \alpha \le 2\pi \end{cases} \tag{9}$$

or

$$\begin{cases} \rho(\alpha) = R_e & \text{for} \quad 0 \le \alpha \le \alpha_1 \\ \rho(\alpha) = R_e + r_d - a_d - \sqrt{r_d^2 - \left(f_d \frac{\alpha}{2\pi} - f_d + \sqrt{a_d(2r_d - a_d)}\right)^2} & \text{for} \quad \alpha_1 \le \alpha \le 2\pi \end{cases} \tag{10}$$

When dressing overlap ratio $U_d < 1$, it is clear that the AB part of grinding wheel will not be dressed and form a plateau in each wheel rotation.

The variation of dressing overlap ratio will change the wheel peripheral profile, which will in turn change the surface structural pattern. Figure 3 shows the different wheel peripheral cross-sections with the change of U_d value. In Fig. 3, red dash line shows the wheel before dressing, solid line is for the situation of $U_d < 1$, dash line is the situation of $U_d = 1$, and point dot-and-dash line is the situation of $U_d > 1$. It is clear that only part of wheel is dressed when $U_d < 1$. Such wheel profile will create flat gouge bottom during the grinding. In the situation of $U_d = 1$, all wheel periphery is dressed except the points on the helical ridge. The radius of the helical ridge remains the same as the original wheel radius. When $U_d > 1$, original wheel surface will be removed during dressing. The wheel radius becomes smaller than the original one. Some parts of the wheel surface encounter more than one dressing passes as the shadow area shown in Fig. 4a.

In the wheel axial direction, when the dressing overlap ratio $U_d \ge 1$, the wheel surface will replicate the dresser tip profile repeatedly and form a fine wheel topography. The periodical axis pitch distance equals to the dressing feed. The peak-to-valley height (h_s in Fig. 4) after a dressing pass is smaller than dressing depth a_d and can be calculated through the dresser apex radius r_d and dressing feed f_d.

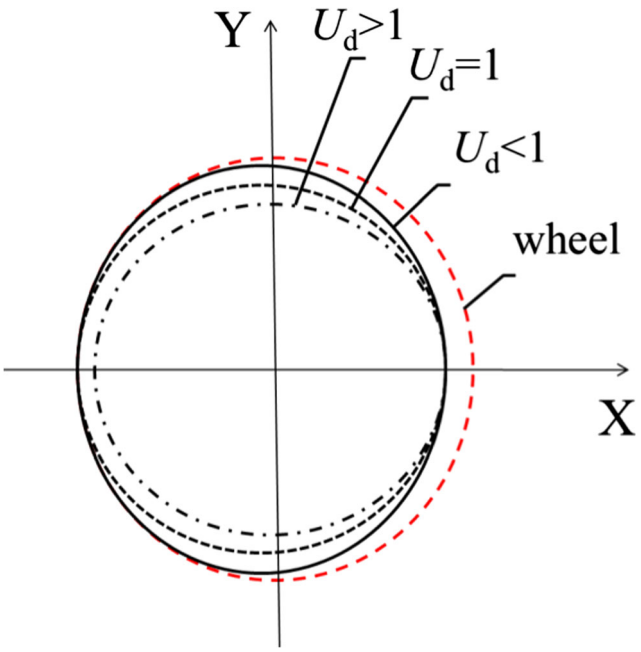

Fig. 3 Generalised wheel peripheral cross-sections with different U_d

$$h_s = r_d - \sqrt{r_d^2 - (f_d/2)^2} \tag{11}$$

Equation 11 shows when the dressing overlap ratio $U_d \ge 1$, the peak-to-valley height h_s is only related to the dressing feed f_d and dressing tip radius r_d, where the dressing depth a_d and dressing width b_d have not explicit influence. When $U_d < 1$, the peak-to-valley height is only related to the dressing depth a_d as the case in Fig. 2.

For the dressing overlap ratio $U_d \ge 1$, the length of undressed wheel surface b in Fig. 2 ($U_d < 1$) has vanished. The local wheel radius in the axial direction can still be established by diamond dresser radius r_d as in Eq. 12. As shown in Fig. 4b, the value of α_1 becomes zero, and wheel surface between α_3 to 2π and 0 to α_2 is cut-in phase and cut-out phase with the workpiece respectively.

$$\rho(\alpha) = R_e + r_d - h_s - \sqrt{r_d^2 - \left(f_d \frac{\alpha}{2\pi} - \frac{f_d}{2}\right)^2} \quad 0 \le \alpha \le 2\pi \tag{12}$$

When $U_d \ge 1$, the feature points C and E on the wheel cross-section are calculated by:

$$\alpha_2 = 2\pi \left(1 - \frac{\sqrt{h_s(2r_d - a_d)}}{f_d} - \frac{\sqrt{(h_s - a_p)(2r_d - h_s + a_p)}}{f_d}\right) \tag{13}$$

$$\alpha_3 = 2\pi \left(1 - \frac{\sqrt{h_s(2r_d - a_d)}}{f_d} + \frac{\sqrt{(h_s - a_p)(2r_d - h_s + a_p)}}{f_d}\right) \tag{14}$$

In order to create the grid pattern on the wheel surface, it requires the dresser to dress the wheel in both forward and backward directions. After the forward dressing, the grinding wheel possesses a single helical groove on its surface. The second dressing in reverse direction starts to engage with the wheel at arbitrary position and produces another helical groove forming a grid structure pattern on the wheel surface. The peripheral cross-section after two dressing

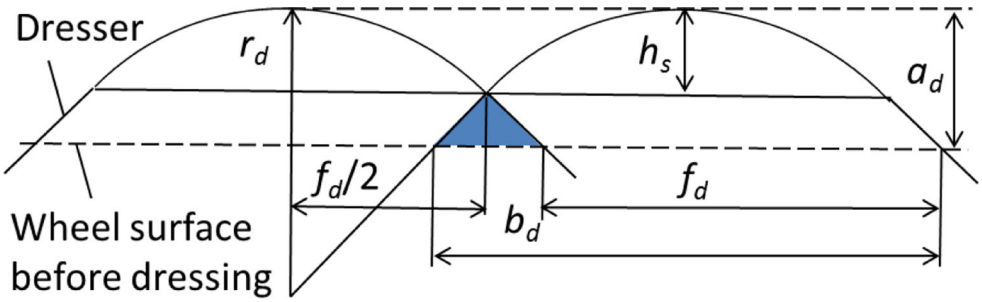

(a) Dressing overlap when $U_d > 1$

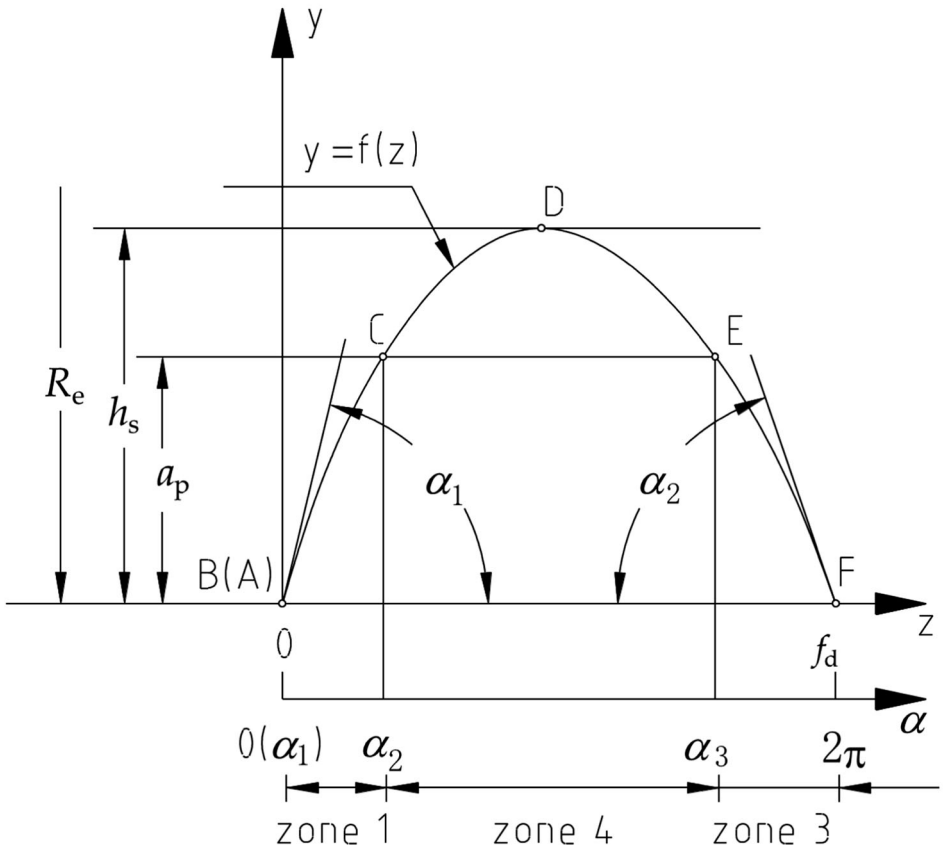

(b) Interaction between dressed wheel and workpiece during grinding

Fig. 4 Axial cross-section profile of dressed wheel when $U_d \geq 1$. **a** Dressing overlap when $U_d > 1$. **b** Interaction between dressed wheel and workpiece during grinding

passes is more complicated. For $U_d < 1$, part of wheel will not be dressed in first dressing, but the existence of zone 2 (between A and B in Fig. 2) could be smaller and may vanish in the second dressing pass depending on the dressing engaging position. The interesting engage position of second dressing is at the half rotation position in the circumferential direction, and the dressing curve is close to the first dressing grove and makes the wheel cross-section area smallest, like an oval shape in Fig. 5. More common situation is that two dressings make the oval shape fatter, but the peripheral cross-section wheel profile is between the smallest oval shape and that formed by one dressing pass. During the grinding, only the two sharp edges of oval wheel will cut through the workpiece. In the situation of $U_d \geq 1$, the situation is nearly the same.

As aforementioned, the choice of microstructure dressing should consider the factors of dressing overlap ratio, dressing feed, dressing tool apex radius, and dresser engage width, which could alter the wheel profile in both axial and peripheral directions.

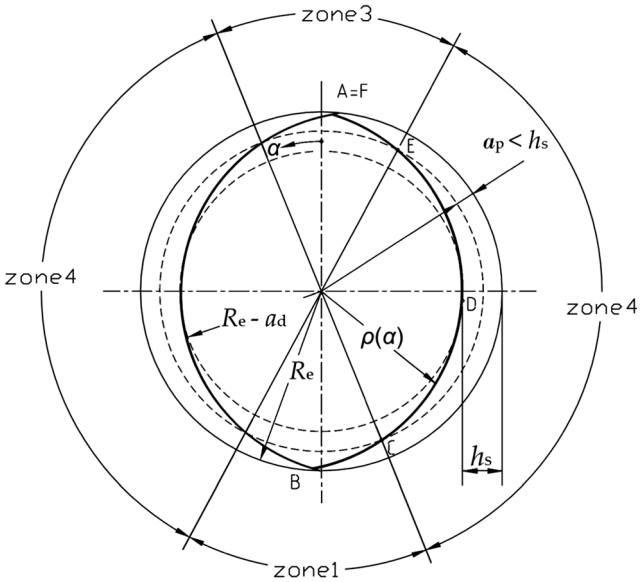

Fig. 5 Peripheral cross-section of the wheel after two dressings

2.2 Microstructural surface creation on workpiece

In the process of microstructural cylindrical plunge grinding, the wheel moves towards the workpiece with radial feed v_f and pulls out at the end of one rotation to finish the grinding size requirement. The dressed wheel will transfer its surface pattern to generate mirrored grid structure on the workpiece. A single microgrinding gouging structure is shown schematically in Fig. 6.

It is understandable that the microstructural feature is decided by the pattern wheel and grinding parameter, especially grinding depth a_p that defines the depth of microstructural gouge depth. Control grinding depth will not only affect the grinding performance and workpiece quantity, but also control the microgrinding structure size.

The pattern size of ground surface structure can be calculated from the wheel surface pattern and the grinding depth. The structural pattern texture is the reproduction print of the wheel surface pattern with grinding depth in speed ratio. The grinding depth affects the feature of the surface structure gouges in all three dimensions: depth, width, and length.

The structure width can be calculated along the dressing direction by establishing the equation with dresser shape. As shown in Fig. 7, the maximum width of gouged structure b_w for $U_d \geq 1$ is directly related to the wheel surface pattern and grinding depth a_p and its size will not exceed the dressing feed.

$$b_w = f_d - 2l_x = f_d - 2\sqrt{r_d^2 - (r_d - h_s + a_p)^2} \tag{15}$$

where l_x is uncut length of workpiece that is calculated based on the geometrical relation illustrated in Fig. 7.

$$l_x = \sqrt{r_d^2 - (r_d - h_s + a_p)^2} = \sqrt{(h_s - a_p)(2r_d - h_s + a_p)} \tag{16}$$

In fact, the width in Eq. 15 is the function of dressing feed f_d, grinding depth a_p, and dresser tip radius r_d. Large dressing feed leads to a large interval of grid structure which will result in large gouge width. It can also conclude that the larger grinding depth will make larger gouge width in the same dressing strategy. But the limitation of microstructural grinding is the h_s that constrains the grinding depth. It should be noted that tip radius and feed rate have influence on the actual peak-valley height h_s as in Eq. 11 and the structure width as in Eq. 15. While a smaller dresser tip radius will lead to a larger gouge width, the feed rate is the most decisive factor that affects structural features in axial direction.

Similarly, the gouge length is determined by those active grains that scratch along the cutting direction. After one reciprocated dressing, the wheel cross-section profile turns into an olive shape as shown in Fig. 5. The corresponding situation is that only grains located in zone 1 and zone 3 will cut

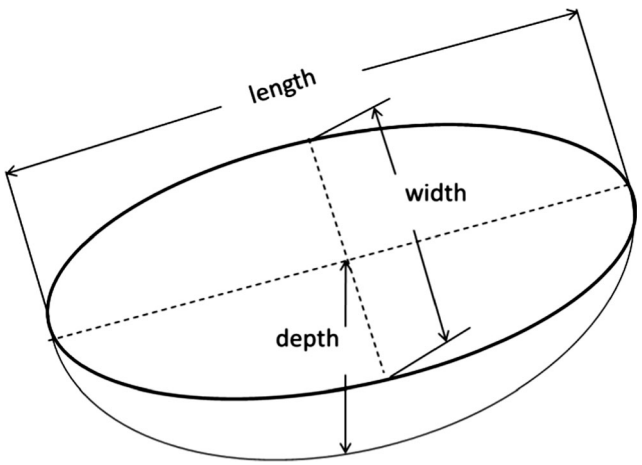

Fig. 6 Schematic views of single microgrinding gouging structure

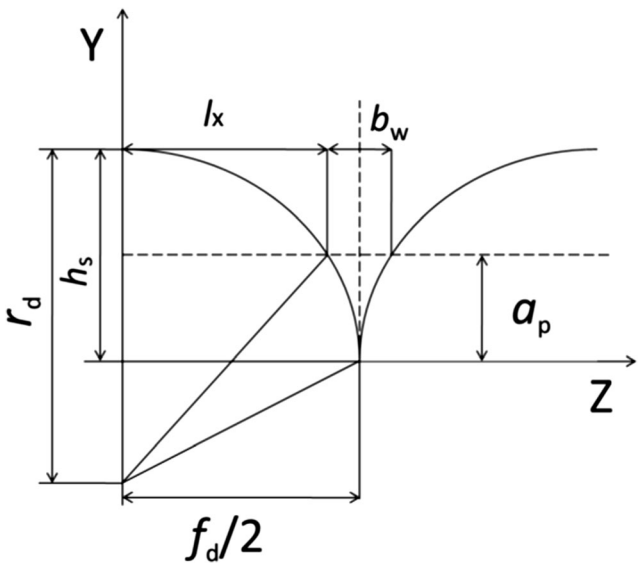

Fig. 7 Schematic views of b_w calculation based on dressing tip radius

workpiece following grinding cycloid trajectory. The grains located in zone 2 and zone 4 will not engage with workpiece material because $\rho(\alpha) < R_e - a_p$, which leaves plateaus along the cutting direction on the workpiece surface.

During the cylindrical grinding, the pattern wheel infeed the workpiece with grinding depth. Meanwhile, the workpiece patterns will be scaled in the circumferential direction by the speed ratio $q = v_w/v_s$ between workpiece and wheel. The workpiece will move forward a length of longitudinal pitch L during one wheel revolution. The circumferential pitch of the workpiece structure will be:

$$L = 2\pi R_s q = v_w/n_s = 2\pi R_w \times n_w/n_s \tag{17}$$

where R_w is the radius of workpiece, n_w is the rotational speeds of workpiece, and n_s the rotational speeds of grinding wheel. The ratio of n_s/n_w is the rotational speed ratio p, which is an important parameter in microstructural surface grinding.

For plunge grinding, the structural gouging texture can be regarded as the result of dressed wheel imprint its surface pattern on to the workpiece surface with grinding depth. From Eq. 17, it can be seen that the workpiece periphery is p times of the pitch length L. Therefore, an integer value of rotational ratio p is necessary for the structure pattern on the workpiece without overlap. The non-integer value of rotational ratio p in plunge grinding will make ground microstructure destroyed by next revolution of grinding. In order to create defined microstructural surface, it is necessary to control workpiece rotational speed to meet the integer requirement of p value.

When active grains on the wheel surface scratch in the cutting direction, a gouge will be created and those uncut parts of workpiece surface will remain as plateaus on the workpiece. The grains on the active part of wheel create the workpiece texture in the axial and peripheral directions simultaneously. The gouge width is the cutting scratch in axial direction, while gouge length is the cutting scratch in peripheral direction. Therefore, the proportion of gouge length in a grid pitch length should be the same as the proportion of gouge width in a dressing feed. As the result, the gouge length and width can be expressed as:

$$l_w = L \times \left(1 - \frac{2l_x}{f_d}\right) = L \times \left(1 - \frac{2\sqrt{r_d^2 - (r_d - h_s + a_p)^2}}{f_d}\right) \tag{18 - a}$$

$$b_w = f_d \times \left(1 - \frac{2l_x}{f_d}\right) = f_d \times \left(1 - \frac{2\sqrt{r_d^2 - (r_d - h_s + a_p)^2}}{f_d}\right) \tag{18 - b}$$

Equation 18-a and 18-b shows that the same ratio l_x/f_d is applied to the calculation of the length and width of gouge generation. The difference between them is the magnitude of the gouge length and width, and gouge length is largely decided by the pitch length L while gouge width is largely decided by the feed rate f_d. The cutting part ratio in two directions is the same. It also shows that gouge length l_w is related to grinding depth a_p, nominal peak to valley height h_s, tip radius r_d, and dressing feed f_d. The equation illustrates that gouge length and width can be controlled by grinding parameters together with dressing strategy. Comparing Eqs. 15 and 18-b, it can be seen that the gouge widths calculated from wheel axial profile or peripheral profile uncut ratio are the same.

When considering the situation of $U_d < 1$, the gouge width can use the same method to calculate its value through an uncut ratio f_{uc}, which is defined as the proportion of inactive part of the wheel in one wheel periphery. The CE part of the wheel shown in Fig. 2 or Fig. 4 is the inactive part of dressed grinding wheel that will not engage with workpiece in grinding. The uncut ratio can be calculated by the following formulas deduced from Eqs. 6 and 7 for $U_d < 1$ and Eqs. 13 and 14 for $U_d \geq 1$.

$$\begin{cases} f_{uc} = \dfrac{(\alpha 3 - \alpha 2)}{2\pi} = \dfrac{2\sqrt{(a_d - a_p)(2r_d - a_d + a_p)}}{f_d \pi} & U_d < 1 \\ f_{uc} = \dfrac{(\alpha 3 - \alpha 2)}{2\pi} = \dfrac{2\sqrt{(h_s - a_p)(2r_d - h_s + a_p)}}{f_d \pi} & U_d \geq 1 \end{cases} \tag{19}$$

During grinding, only active part of the wheel will cut into the workpiece and generate gouges. Using uncut ratio, the maximum width in the axial direction can be calculated as:

$$\begin{cases} b_w = f_d(1 - f_{uc}) = f_d \times \left(1 - \dfrac{2\sqrt{(a_d - a_p)(2r_d - a_d + a_p)}}{f_d}\right) & U_d < 1 \\ b_w = f_d(1 - f_{uc}) = f_d \times \left(1 - \dfrac{2\sqrt{(h_s - a_p)(2r_d - h_s + a_p)}}{f_d}\right) & U_d \geq 1 \end{cases} \tag{20}$$

Similarly, the length of gouge can be calculated as:

$$\begin{cases} l_w = L(1 - f_{uc}) = L \times \left(1 - \dfrac{2\sqrt{(a_d - a_p)(2r_d - a_d + a_p)}}{f_d}\right) & U_d < 1 \\ l_w = L(1 - f_{uc}) = L \times \left(1 - \dfrac{2\sqrt{(h_s - a_p)(2r_d - h_s + a_p)}}{f_d}\right) & U_d \geq 1 \end{cases} \tag{21}$$

Equation 21 demonstrates the gouge length is related to grinding depth a_p, dressing depth a_d, tip radius r_d, and dressing feed f_d. It is interesting to note that the dressing depth is an

explicit influential factor on gouge size when $U_d < 1$, but became insignificant when $U_d > 1$. The reason is that all original wheel surfaces have been dressed when $U_d > 1$ and dressing depth becomes irrelevant.

Equations 20 and 21 are deduced based on the geometry of dressed wheel. They reveal the interaction between the wheel and workpiece during grinding, which explains the textural gouge generation in the sense of geometrical engagement.

2.3 Surface texture formation in considering grinding kinematics of individual grit

Due to the complex phenomena in the grinding zone, arbitrary-orientated grains and the elastic and plastic deformation in grinding will affect the patterned gouge formation. Chen et al. [37, 39–41] demonstrated the workload on abrasive grit is the core issue in grinding process modelling and simulation. The formation of ground surface is the aggregation of the actions of all individual abrasive grits in the grinding wheel. Since the formation of textural surface directly relates to individual grit kinematics, the grit moving trajectory model should be established to help the understanding of the surface pattern formation. Therefore, the influence of the variation of each active grain, grinding direction, and wheel-workpiece contact constraint in microstructure creation should be analysed.

The geometric or kinematic relationship between the wheel surface pattern and workpiece in grinding dominates the size and shape of gouges. The models presented by Eqs. 20 and 21 are based on geometrical engagement between dressed wheel and workpiece. For each grit on grinding wheel surface, it will follow a cycloid path along the workpiece to remove the materials at the front of the grit. The grit cycloid path is illustrated in Fig. 8, which reveals the kinematics relation in grinding. In the cutting direction, the cutting path of each grit is the fundamental mechanism of texture surface formation determined by the grit polar angular position in relation to grinding kinematics and dressed wheel surface pattern. The aggregation of all grit cutting paths on the workpiece will result in the final structural texture of ground surface. The gouge shapes at the cut-in and cut-out sections are determined by the trajectory of individual grit paths.

Each of abrasive grains in the grinding wheel has a peripheral position angle α in the polar coordinate. During grinding, only outmost grains in active wheel part will cut the workpiece. It is assumed that the wheel rotates counterclockwise with rotational angle φ. In Fig. 8, the wheel rotational position is illustrated in the same space as the wheel polar angular space α to describe the abrasive grains gradually cut into the workpiece at an equal interval angle to form the texture. As shown in Fig. 8, the corresponding positions $\alpha 2$ and $\alpha 3$ of active wheel are x_{ex} and x_{en} in the grinding path respectively. In the model, the imaged rolling line is regard as the grinding wheel rolls forward on the workpiece. For cylindrical grinding, the radius of imaged wheel can be expressed as:

$$r = R_e q = \frac{R_s R_w}{R_s + R_w} \times v_w / v_s \tag{22}$$

where R_e is the equivalent radius of grinding wheel.

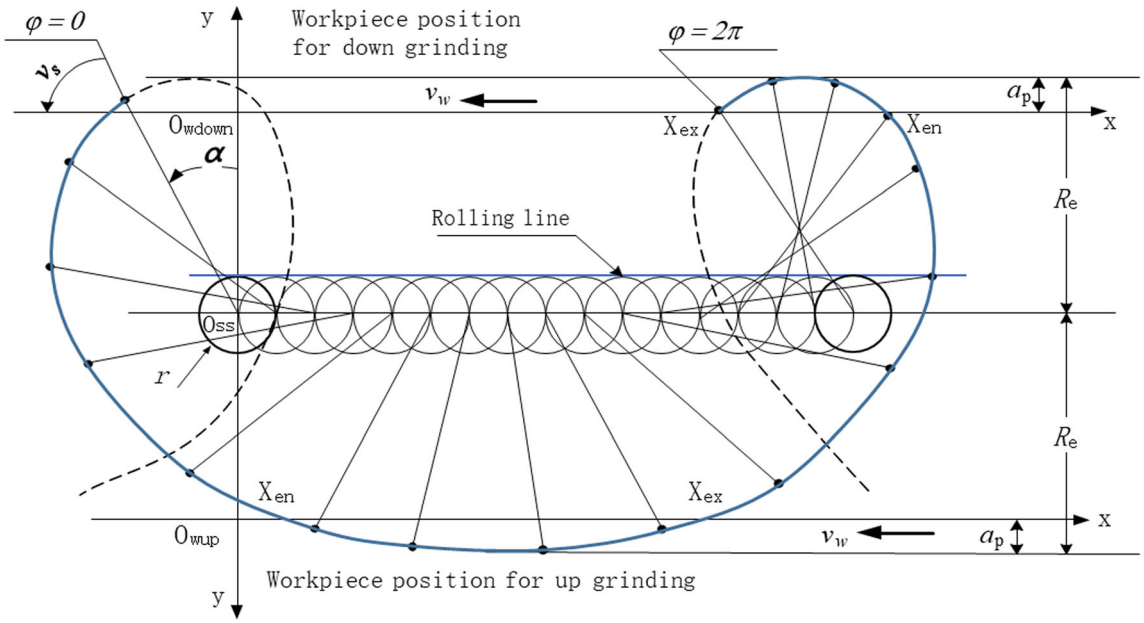

Fig. 8 Cycloid path of grains for down- and up-grinding

Considering different situations of up- and down-grinding, the grits on the wheel active surface cut into the workpiece and move over a cycloid path in the related coordinate system (i.e. O_{wup} or O_{wdown} in Fig. 8 for up- or down-grinding) connected with the work material. The grain paths in Fig. 8 are expressed in Eq. 23-a for up-grinding and Eq. 23-b for down-grinding:

For up-grinding:

$$\begin{aligned} x &= r\varphi - \rho(\alpha)\sin(\alpha+\varphi) \\ y &= \rho(\alpha)\cos(\alpha+\varphi) - a_p + R_e \end{aligned} \quad (23-a)$$

For down-grinding:

$$\begin{aligned} x &= r\varphi - \rho(\alpha)\sin(\alpha+\varphi) \\ y &= \rho(\alpha)\cos(\alpha+\varphi) + a_p - R_e \end{aligned} \quad (23-b)$$

For each active grain, located at the radius $\rho(\alpha) > R_e - a_p$, it will cut into the work material at the angle φ_{en} and leaves at angle φ_{ex}. Angles φ_{en} and φ_{ex} of wheel rotation can be calculated by substituting $y = 0$ in Eq. 23. This enables the determination of the abscissas x_{en} and x_{ex} of entrance and exit points:

For up-grinding:

$$\begin{aligned} \varphi_{en} &= \arccos\left(\frac{a_p - R_e}{\rho(\alpha)}\right) - \alpha \\ \varphi_{ex} &= 2\pi - \arccos\left(\frac{a_p - R_e}{\rho(\alpha)}\right) - \alpha \end{aligned} \quad (24-a)$$

For down-grinding:

$$\begin{aligned} \varphi_{en} &= -\arccos\left(\frac{R_e - a_p}{\rho(\alpha)}\right) - \alpha \\ \varphi_{ex} &= \arccos\left(\frac{R_e - a_p}{\rho(\alpha)}\right) - \alpha \end{aligned} \quad (24-b)$$

To calculate the longest grit gouging length, the largest radius of grit position in the grinding wheel should be considered. The α value corresponding to the largest radius of the wheel surface is 0 when $U_d \geq 1$ or in the range of $0 \sim \alpha_1$ when $U_d < 1$. For the cases under consideration, the largest $\rho(\alpha)$ is the R_e of the dressed wheel. Therefore, substituting these values in Eq. 24, the longest grit gouging length can be deduced from the kinematic model:

For up-grinding:

$$l_{wk\text{-}up} = x_{ex} - x_{en} = r\left[2\pi - 2\arccos\left(\frac{a_p - R_e}{R_e}\right)\right] + 2R_e\sin\left[\arccos\left(\frac{a_p - R_e}{R_e}\right)\right] \quad (25-a)$$

For down-grinding:

$$l_{wk\text{-}down} = x_{en} - xn_{ex} = r\left[-2\arccos\left(\frac{R_e - a_p}{R_e}\right)\right] + 2R_e\sin\left[\arccos\left(\frac{R_e - a_p}{R_e}\right)\right] \quad (25-b)$$

Equation 25 shows the maximum grit gouging lengths are different with up- or down-grinding. However, the maximum gouge widths are the same for both up- and down-grinding, because the gouge width is orthogonal to grinding cutting direction.

Although the gouge dimensions calculated from kinematic model describe the structural surface formation in detail, it may not fully illustrate the formation of final ground surface creation due to the complex grinding contact phenomenon in the grinding zone. The final gouge shape is determined by the outmost profile of all grit paths passed the workpiece, which means the final gouge length is affected by the individual grit path, texture pitch length, and grinding contact length.

In Fig. 9, two different cases are illustrated to demonstrate the influence of contact length on the texture formation. Individual grit grinding path follows cycloid curve to cut through workpiece. The aggregation of these cutting paths generates the gouges on the workpiece surface. The gouge models Eqs. 23~25 reflect the texture generation when their sizes are smaller than the pitch length. In grinding, the maximum grit gouging length will not exceed the pitch length, because the texture pattern will repeat in next pitch length.

The grinding contact length is a function of the speed ratio $q = v_w/v_s$, grinding depth of cut a_p, and radius of grinding wheel and component [37, 39, 41, 42]. A simple grinding contact model is the kinematic contact length l_k that can be presented as

$$l_k = (1 \pm q)\sqrt{2R_e a_p} = \left(1 \pm \frac{v_w}{v_s}\right)\sqrt{2\frac{\rho(\alpha) r_w a_p}{\rho(\alpha) + r_w}} \quad (26)$$

where the plus sign is for the up-grinding and minus sign is for the down-grinding.

Along the cutting direction, if the double grinding contact length or gouge length is larger than the pitch length, all original workpiece surface will be removed as the case b in Fig. 9. The texture feature will repeat cyclically in each pitch length that should always be longer than each texture gouge length. Because the contact length is the length that wheel engaged with workpiece, it is impossible to create a gouge with a depth of a_p and its length shorter than the double grinding contact length. Therefore, during design of grinding surface texture, the constraints of pitch length and grinding contact length should be considered.

3 Experiments of microstructural surface creation

The dressing and grinding experiments were carried out on a Jones shipman cylindrical grinding machine. An alumina grinding wheel 77A601J8V of 60 mesh size was used for

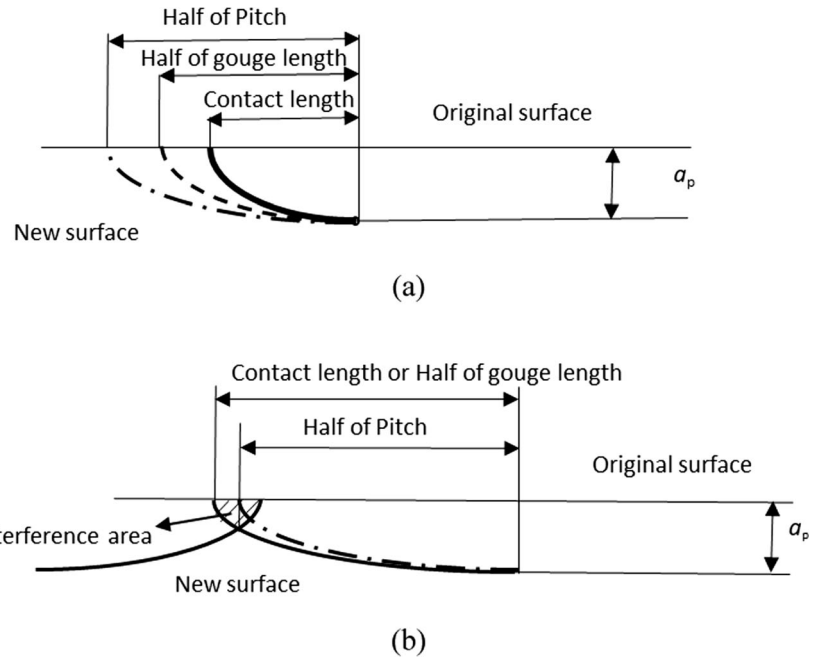

Fig. 9 Contact length influence on the texture formation. **a** Pitch length is longer than the gouge length and the double grinding contact. **b** Pitch length is shorter than the gouge length or the double grinding contact

the experiments. The wheel surface pattern was generated on the wheel surface by dressing the wheel forward and backward at the same depth of cut. The dressing operation was carried out using a chisel diamond dresser with active radius estimated as 1.027 mm. The diamond dresser profile measurement and its profile curve fitting are shown in Fig. 10. The dressing and grinding were executed under constant wheel spindle rotational speed (1665 rpm). The grinding wheel diameter was measured as 412 mm and the workpiece diameter was 40.2 mm. The workpiece material is carbon steel. Prior to the grinding tests, workpieces were prepared by polish grinding to get smooth surface (Ra around 0.07 μm). Acoustic emission monitoring was applied to ensure only one grinding revolution without overlap. The detailed experimental conditions are shown in Table 1.

After grinding, the surface textures of workpieces were measured by using stylus contact methods and optical non-contact methods. The feature extraction methods are the same as the methods explained in the literature [42]. A Wyko (RST-Plus Optical Profiler) white light interferometer was used to measure and assess the features of the textured profiles. After obtaining 3D texture profiles, the 2D surface profiles in different directions are extracted from the deepest point of the texture to measure the groove depth, groove length, flat length, and other relevant texture information. The deepest point of grain paths is generally at the middle of gouge patterns, but sometimes due to the imperfection of workpiece surface or the position offset of grains, the deepest point of the groove could deviate from the middle of the gouge patterns. Further, the gouge patterns were compared to establish relations for the model validation.

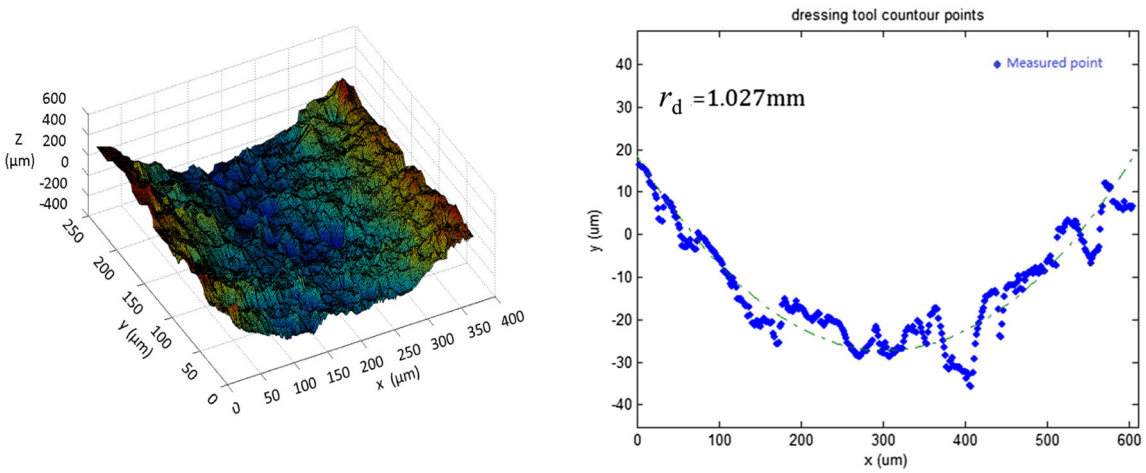

Fig. 10 Dressing tool measurement result and radius fitting

Table 1 Experimental conditions

Test no.	a_d (μm)	f_d (μm/rev)	v_s (m/s)	n_s (rpm)	n_w (rpm)	a_p (μm)	V_f (mm/min)	U_d
A	10	340	35	1665	10	6	0.06	0.83
B	20	340	35	1665	10	6	0.06	1.17
C	20	340	35	1665	10	2	0.02	1.17

4 Feature assessment of microstructural surface

Grinding texturing is the combination of dressing and grinding operations. The ground surface topography not only shows the regular shape, size, and distribution of structural texture, but also reflects grinding performance like texture formation, grain cutting characteristics, and the elastic deformation in grinding. The dressing operation creates a regular pattern structure on the top of the

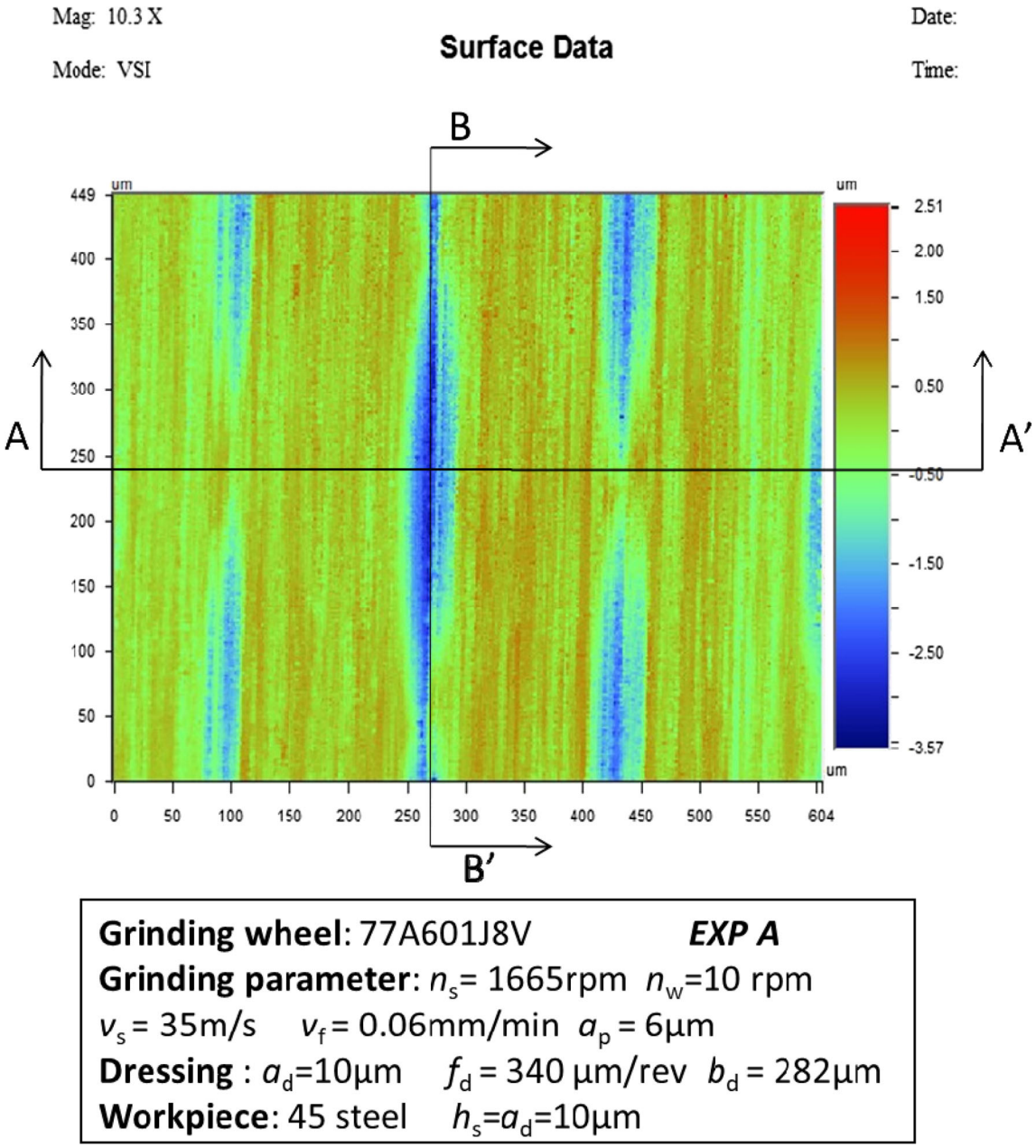

Fig. 11 Topography of ground surface of test A

wheel surface, which is made of randomly positioned irregular abrasive grits. With such a patterned wheel with irregular grain shapes, the ground surface will possess regular pattern with random microstructural details. The topography of ground surface textures from texts A, B, and C is shown in Figs. 11, 12, and 13, respectively, where the plateau in red is the top surface of the workpiece created from previous polish grinding and the blue gouges with regular position pattern are the surface microstructures created by grinding texturing.

4.1 Surface topography analysis in workpiece axis direction

Figure 14 shows axial direction profiles extracted from the 3D surface topography in dressing feed direction, which reflects the dresser profile and dressing feed. The top plateau part is original surface before texture grinding and the valley part is the gouge groove. The interval of groove is nearly 340 μm, which is the dressing lead. Although the gouge valley profile reflects the dresser cross-section profile, the variation of the

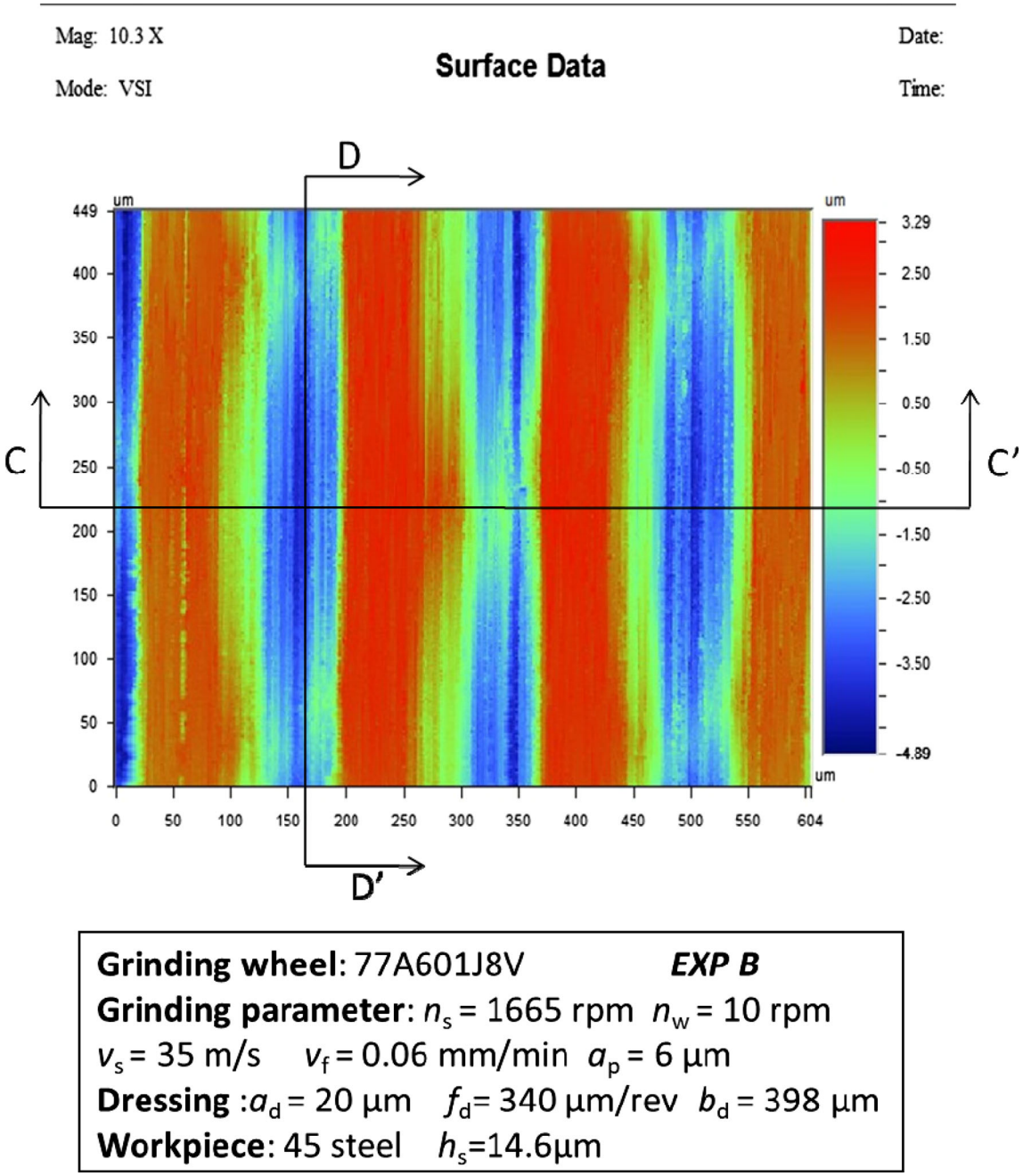

Fig. 12 Topography of ground surface of test B

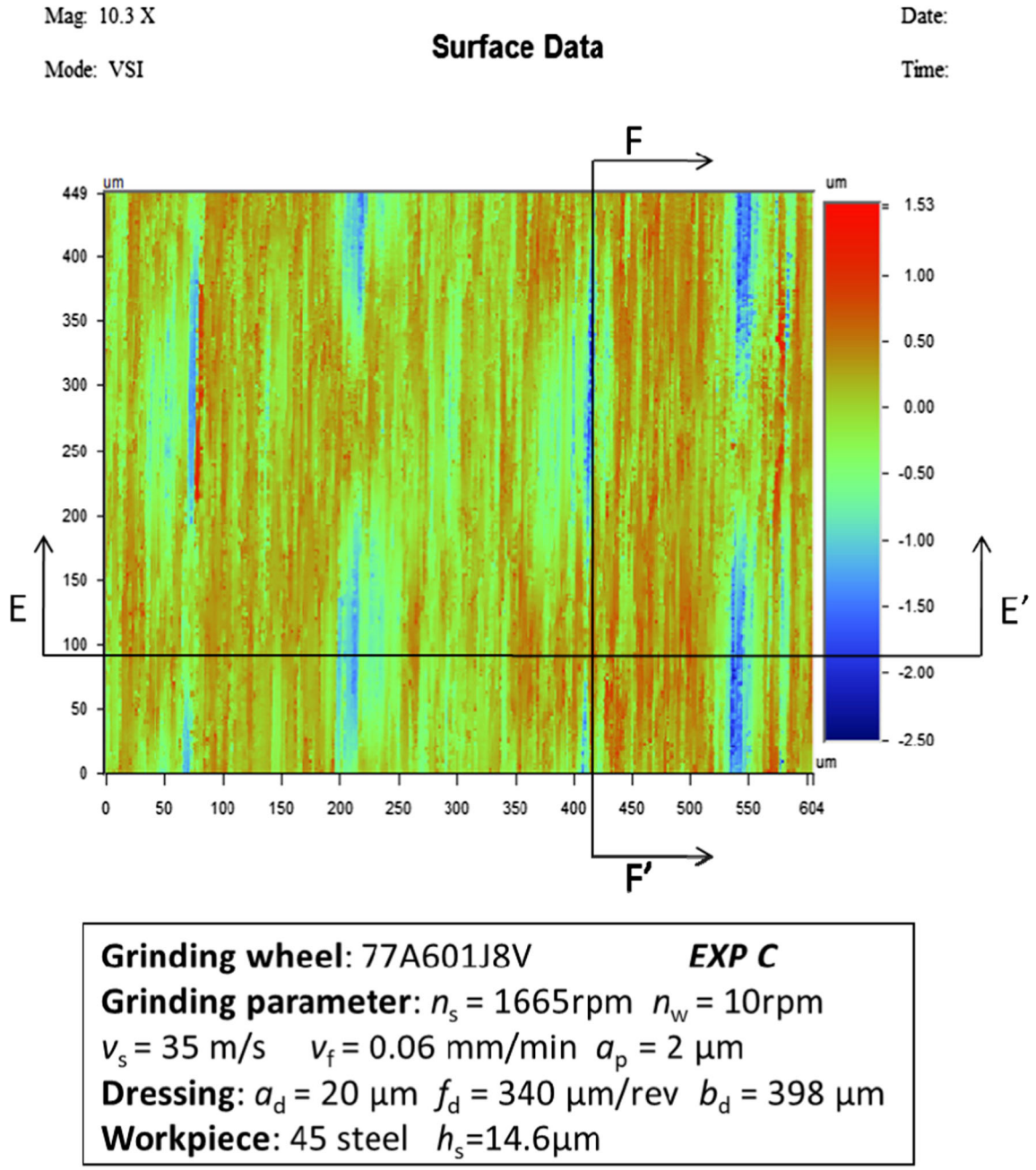

Fig. 13 Topography of ground surface of test C

profiles is obvious. This is because a dressing operation fractures grains on the wheel surface leaving only a few surface points of each grain to be consistent with the dresser cross-section profile. Each grain cutting does not present the dresser cross-section profile. However, those outmost cutting edges of all active grains on the wheel surface work together will recreate the feature of the dresser cross-section profile on the gouge texture.

As shown in Figs. 11 and 14a (A-A), the width of the flat at the top of workpiece surface is nearly 290 μm and the groove width is 40–50 μm. The active part of the pattern wheel gouges through the workpiece forming a groove of depth 3.6 μm that is smaller than the set grinding depth of cut 6 μm. Such difference may be due to setting error or the deflection of the grits that engaged with the workpiece. In order to reveal the effects of grinding depth of cut, further theoretical analysis will base on the measured value.

In Fig. 12, the width of plateau at section C-C is nearly 220 μm and groove width is around 120 μm. The depth of groove is deeper than that of in test A because the dressing depth is doubled. The larger dressing depth normally reduces the density of cutting edged on the wheel surface leading to lower grinding force and less deflection of grits [39, 42]. Here, the groove depth ground by the pattern dressed wheel

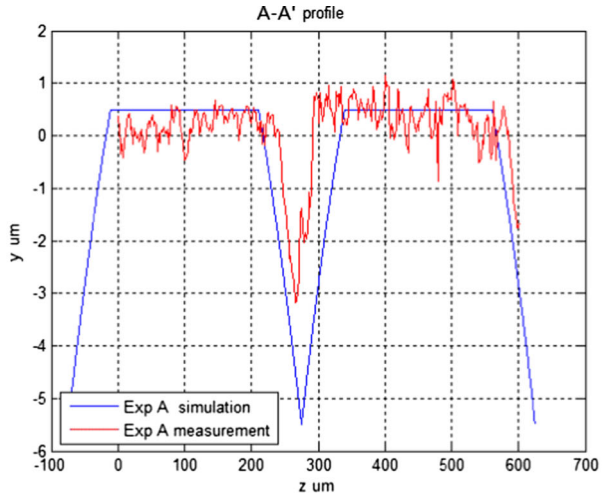

(a) Test A

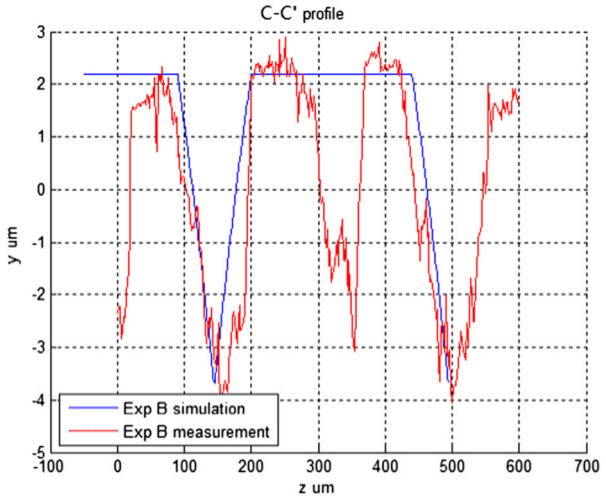

(b) Test B

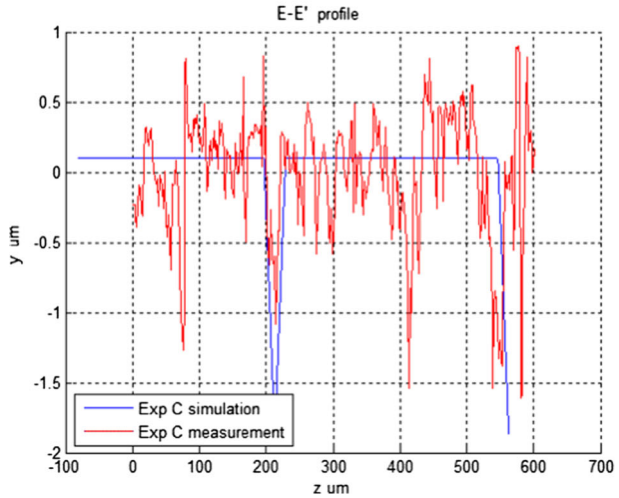

(c) Test C

Fig. 14 Simulation and measurement of cylinder workpieces along axis direction. **a** Test A. **b** Test B. **c** Test C

becomes close to the set grinding depth of cut 6 μm. Compared with test A, it can be seen that larger real grinding depth of cut leads to larger gouge width. Further, the larger U_d will make h_s smaller, which also leads larger gouge width.

In Fig. 13, the gouge layout is similar to that in Fig. 11 but gouge depth is smaller due to a smaller grinding depth of cut that is applied. The width of the flat at the top of the plateau in Fig. 14c is nearly 310 μm and average groove width is 20–30 μm. In Fig. 14b, c, another groove also appears in the middle of the dressing feed. This happens because the dual direction dressing operation would introduce another set of gouges in the middle of the first set of gouges with a shifted angle. If the gouge length is long enough, both sets of gouges will appear in the same cross-section.

By comparing the topography of three tests, it is noted that the groove depth can mainly be controlled by grinding depth of cut. The larger the grinding depth of cut, the larger the groove depth. Figure 15 shows the comparison of gouge width value between the model calculation and the measurement in the tests A, B, and C. In the same dressing condition of tests B and C, the small grinding depth makes the gouge width smaller, which is the same as expressed in the model Eq. 20. As it can be seen in Fig. 14 that actual cutting depth may not be the same as the nominal one, so the gouge width may vary from the model value. The differences between the model and measurement are affected by the elastic and plastic deformation or the grit distribution on the wheel surface. The dressing condition has strong influence on the effects of grinding depth on gouge width. One big difference between tests A and B is dressing overlap ratio U_d. When $U_d \geq 1$, larger U_d will decrease the h_s, which leads to larger gouge width. However, both theory and experiment show that the texture features along the component axis direction are dominated by dressing feed and diamond apex profile.

4.2 Surface topography analysis in workpiece circumferential direction

Figure 16 shows the texture profiles in cutting direction extracted from 3D surface topography. The cutting direction is

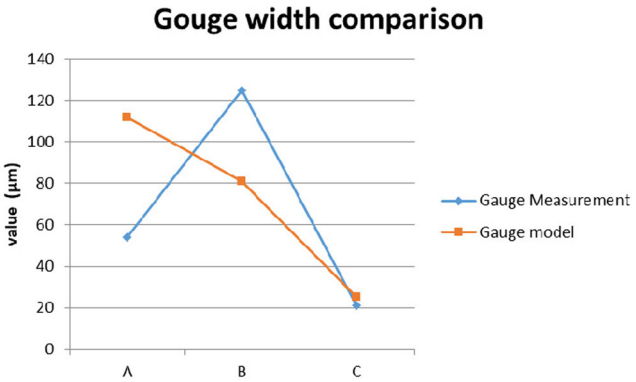

Fig. 15 Texture gouge width comparison of tests A, B, and C

from left to right, and all the actual gouge profiles have the trajectory curve close to the ideal cycloid shape.

Although the nominal grinding depth of cut is 6 μm in test A and test B, the largest height of actual profiles B-B′ and D-D' are only about 2 μm which are far less than the set depth of cut. It should be noted that the condition of tests A and B is actually the case b in Fig. 9, where theoretical gouge length is longer than the texture pitch length. In such a case, the remained profile cannot present the full cutting trajectory. Looking at Figs. 11 and 12, the real cutting depths are around 5 μm for test A and 7 μm for test B, which means the grinding gouges actually form slots on the workpiece surface. Figure 16a, b actually shows the bottom profiles of these slots. The pitch length is a dominated feature of these slot profiles. In test C, the nominal depth of cut is 2 μm and the measured gouge depth is about 1.7 μm. Such a difference may contribute to grinding elastic deformation or machine setup. The measured gouge length is 320 μm that is smaller than the pitch length. Therefore, a plateau appears on the actual gouge profile.

The patterns of structural gouges can be clearly seen from Figs. 11, 12, and 13. The length of gouge can be measured by extracting the profiles in cutting direction as shown in Fig. 16. The measured gouge length value is the distance from the gouge cut-in position to the position of gouge cut-out. The comparison between the measured values and theoretical models is shown in Fig. 17, where the gouge length measurement, geometry gouge model, kinematic gouge model, grinding kinematic contact length, and longitudinal pitch length are illustrated together. In order to allow model to illustrate the real situation in experiment, the real depth of cut is considered in the model calculation. It is clear that the maximum grit gouging length predicted by kinematic model (Eq. 25 represents the outmost grit path) is longer than that by geometrical model (up-grinding in this case). The grit gouging length predicted by kinematic gouge model does not present dressing influence. Geometry gouge models show the influence of U_d. When $U_d > 1$, the influence of dressing depth disappears because the h_s is not a function of dressing depth. While under the same dressing condition, both theoretical models and experiments show the grinding depth of cut has strongly influence to the gouge length as in the cases of test B and test C.

From the section of C-C′ section in Figs. 12 and 14b, it can be seen that the original top surface along the gouge cutting direction is removed due to larger dressing depth applied, where the U_d becomes larger than 1. According to Eq. 25, the longest grit cutting path becomes longer than pitch length as shown in Fig. 17. This is the case shown in Fig.9b where the gouges link together forming a slot. Because the texture patterns will repeat in every pitch length, it can conclude that the gouge length will not exceed the grinding pitch length. As shown in Fig. 5, two apices exist in a wheel cross-section, and the length of the gouge can only up to a half of the pitch length. The measured gouge lengths appear to be in the range

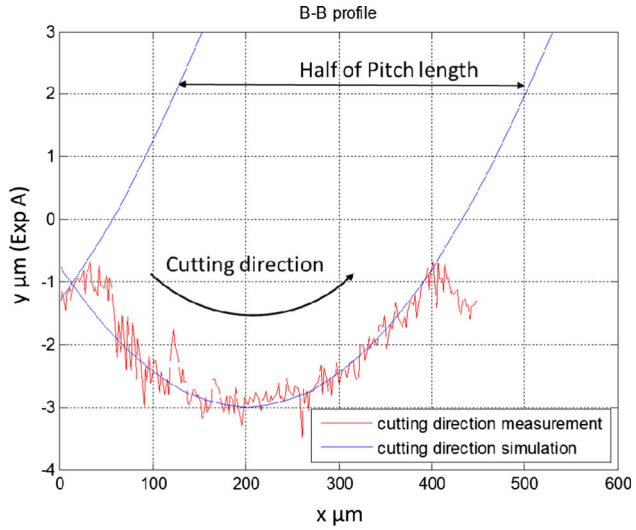

(a) Test A

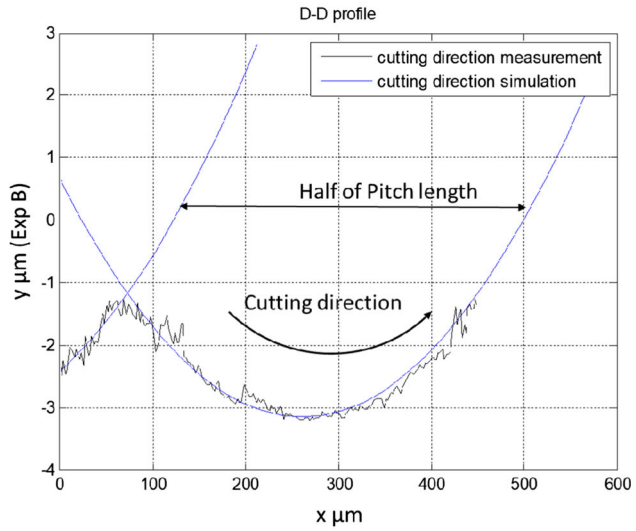

(b) Test B

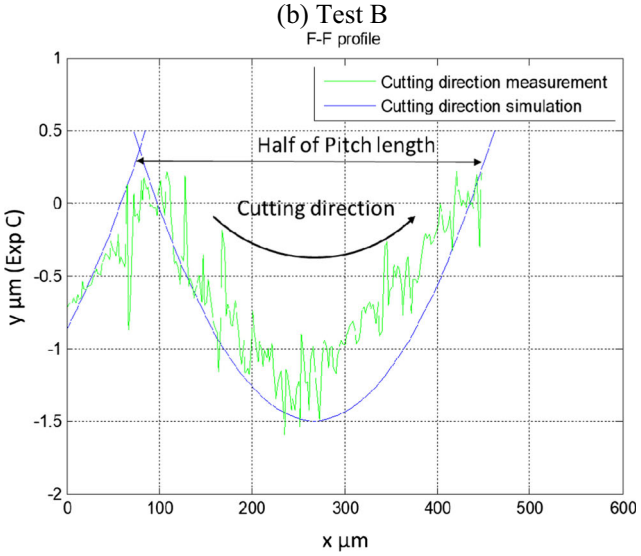

(c) Test C

Fig. 16 Profile comparison between simulation and measurement along cutting direction. **a** Test A. **b** Test B. **c** Test C

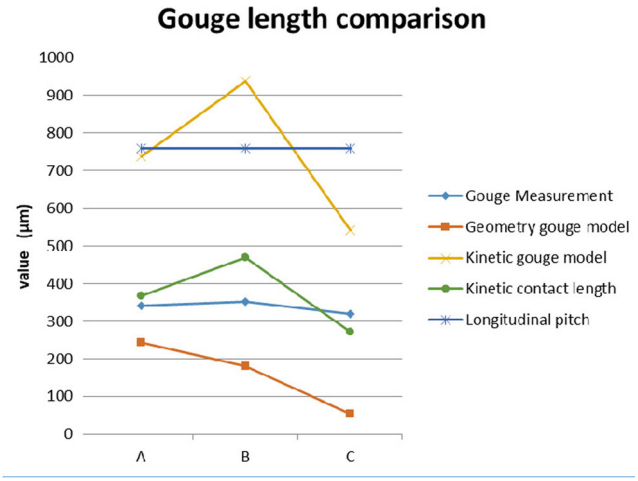

Fig. 17 Structure length comparison of tests A, B, and C

between the values given by the geometrical and kinematic gouge models. The variation of actual gouge length is due to the influence of grit position variation and grinding elastic and plastic deformations.

As it can be seen in the experimental results (shown in Figs. 11, 12, and 13), a certain proportion of surface of workpieces remains un-cut during grinding texturing forming texture plateaus. Textural gouge arrays appear with regular interval. Comparing the profile features in cutting direction and axis direction, it shows that the features in the axis direction are more deterministic with regular interval of flats and grooves. The deterministic texture interval relates closely to the dressing lead. By measuring five different gouges extracted from the ground surface, the standard deviations of gouge widths of tests A, B, and C are 3.51, 4.57, and 1.70 μm, respectively, which are less than 10% of their size. This means the variations of gouge width are acceptable for the texturing operation. However, the profile along the cutting direction shows a significant variation, which is due to each individual grit position that has significant influence on its path in the gouge formation along the cutting direction. There are clearly evidences that the shape of gouge varies due to the variations of influential factors including elastic and plastic deformation, random nature of cutting edge shape, and grain position distribution. The grinding material removal mechanism — rubbing, ploughing, and cutting of individual grinding abrasives, also causes the distortion of the texture profiles [43]. The wear of abrasive grains during grinding could further alter the gouge profile from its normal shape. These influential factors require further investigation for the improvement of the quality of texturing.

4.3 Texture waviness

Another feature of structure surface that has to be considered is the waviness of the cylinder component, which shows how the structures are uniformly distributed around along the circumference of the workpiece. Figure 18 shows the waviness of sample

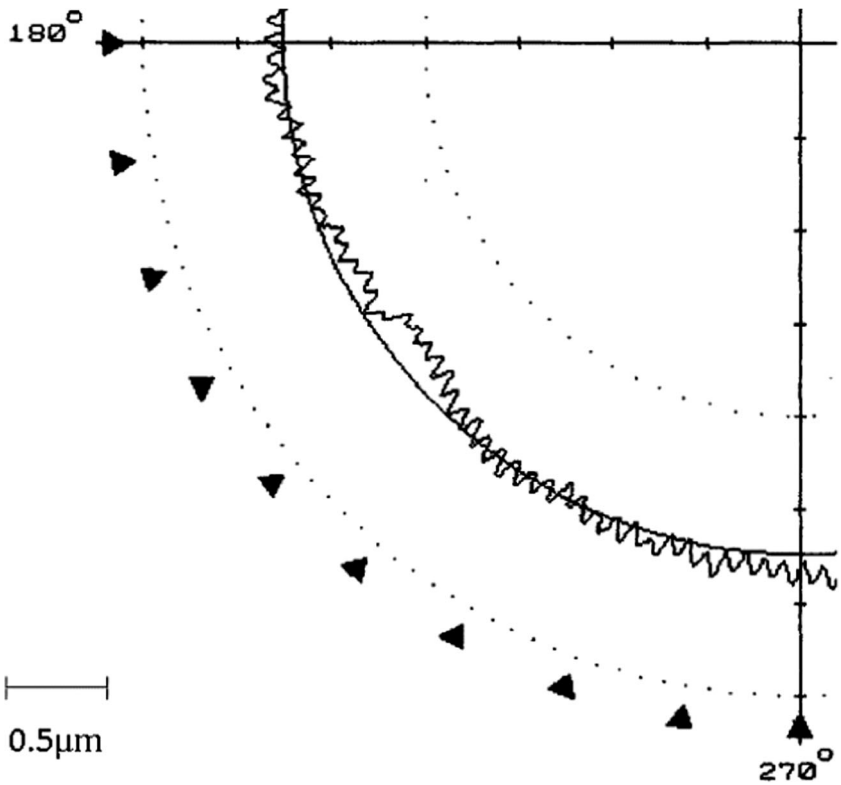

Fig. 18 Part roundness result of test A component

surface from test A, which clearly reflects the structural waviness distribution on the component. The number of the waves depends on the rotational speed ratio $p = n_s/n_w$. From Fig. 18, the texture wave number in one-quarter component is near 41.5, which matches to a quarter of the rotational speed ratio $p =$ 166.5 in test A. The random distribution of grits and grinding burrs could cause the distortion of the waves.

The decimal of rotational speed ratio p means the overlapping of structural texture when more than one revolution grinding operation is taken. The overlapping can ruin the designed surface pattern. Therefore, it is vital to ensure the rotational speed ratio p is integer for cylindrical surface texturing.

5 Conclusion

A set of dressing and grinding models has been developed to illustrate relationship between the features of microstructural surface texture and the operational conditions of dressing and grinding. The formation of cylindrical grinding surface texture is illustrated with the analysis of grinding kinematics. The features of ground microstructure can be depicted by the length and width of grinding gouges and the pitch length in axis and peripheral directions of the cylindrical component. These feature parameters are the functions of dressing and grinding conditions.

With the models presented in the paper, microstructural surface textures can be designed and controlled depending on their pattern requirement. The grinding conditions should be selected in conjunction with wheel dressing conditions. The constraint of textural gouge shape depends on grinding contact length and dressing conditions. When $U_d \leq 1$, the maximum gouge depth is mainly determined by dressing depth; when $U_d > 1$, the maximum gouge depth is determined by both dressing depth and dressing lead. To avoid unexpected interaction between designed texture and process physical constraints, the pitch length of texture pattern in circumferential direction should be larger than grinding contact length. It is noticed that the speed ratio v_w/v_s is an important factor for the pattern layout of the structural surface. The grinding depth affects the structural gouge shape in all three directions: depth, length, and width.

The typical ground surface microstructure models are presented in comparison with experimental measurements. It has demonstrated that the deterministic texture size in the axial direction closely relates to the dressing lead and dresser cross-section shape. Grinding kinematic models govern the grinding gouge shape and length in grinding direction. The textural pitch is determined by dressing lead in axis direction and by grinding speed ratio in peripheral direction. The maximum grinding gouge length cannot exceed the longitudinal pitch length. This important element should be considered in grinding texture design.

Due to the random nature of grit shape and distribution and grinding material removal mechanism, i.e. rubbing, ploughing, and cutting, the profiles of grinding gouges vary away from theoretical curves. The elastic deformation of the grinding system makes the grinding gouge size smaller than that predicted by theoretical models.

The structure gouge number around the workpiece shows high consistency with the model and can be controlled by adjusting rotational ratio. The integer rotational ratio is necessary for plunge cylindrical grinding to produce the microstructure in the same position along the circumference direction and to avoid the texture pattern overlap.

Funding information The research received supports from the Innovation Fund Project for Graduate Student of Shanghai (JWCXSL1401), the Shanghai Municipal Natural Science Foundation (13ZR1428000), the Innovation Program of Shanghai Municipal Education Commission (No. 13YZ068), NSFC (51275201 and 51311130129), China Postdoctoral Science Foundation (201003531), the Royal Society (IE121495), and Marie Curie Actions FP7 (PIRSES-GA-2011-295224).

References

1. Bruzzone AAG, Costa HL, Lonardo PM, Lucca DA (2008) Advances in engineered surfaces for functional performance. CIRP Ann Manuf Technol 57:750–769
2. Stout KJ, Blunt L (2001) A contribution to the debate on surface classifications—random, systematic, unstructured, structured and engineered. Int J Mach Tools Manuf 41:2039–2044
3. Evans C, Bryan J (1999) "Structured," "textured," or "engineered" surfaces. CIRP Ann 48(2):541–545
4. Luo Y, Zhang D (2013) Investigation on fabricating continuous vivid sharkskin surface by bio-replicated rolling method. Appl Surf Sci 282:370–375
5. Dean B, Bhushan B (2012) The effect of riblets in rectangular duct flow. Appl Surf Sci 258:3936–3947
6. Liu KN, Christodoulout C, Ricciust O, Joseph DD (1990) Drag reduction in pipes lined with riblets. AIAA J 28:1697–1698
7. Luo Y, Zhang D (2012) Experimental research on biomimetic drag-reducing surface application in natural gas pipelines. OIL GAS-EUR MAG 38(4):213–214
8. Denkena B, Kohler J, Wang B (2010) Manufacturing of functional riblet structures by profile grinding. CIRP J Manuf Sci Technol 3:14–26
9. Bruzzone AAG, Costa HL (2013) Functional characterization of structured surfaces for tribological applications. Procedia CIRP 12:456–461 8th CIRP Conference on Intelligent Computation in Manufacturing Engineering

10. Andersson P, Koskinen J, Varjus S, Gerbig Y, Haefke H, Georgiou S, Zhmudd B, Buss W (2007) Microlubrication effect by laser-textured steel surfaces. Wear 262(3–4):369–379
11. Dumitru G, Romano V, Weber HP, Haefke H, Gerbig Y, Pflüger E (2000) Laser microstructuring of steel surfaces for tribological applications. Appl Phys A Mater Sci Process 70:485–487
12. Wakuda M, Yamauchi Y, Kanzaki S, Yasuda Y (2003) Effect of surface texturing on friction reduction between ceramic and steel materials under lubricated sliding contact. Wear 254:356–363
13. Ramesh A, Akram W, Mishra SP, Cannon AH, Polycarpou AA, King WP (2013) Friction characteristics of microtextured surfaces under mixed and hydrodynamic lubrication. Tribol Int 57:170–176
14. Ekkard B, Ralf G, Lars S (2012) Review on diamond-machine process for generation of functional surface structures. CIRP J Manuf Sci Technol 5:1–7
15. Yu DP (2012) Optimized tool path generation for fast tool servo diamond turning of micro-structured surfaces. Int J Adv Manuf Technol 63:1137–1152
16. Brecher C, Weinzierl M (2008) Parallel precision alignment of multiple micro components. Microsyst Technol 14:1847–1853
17. Denkena B, Kohler J, Wang B (2010) Advanced microstructures and its production through cutting and grinding. CIRP Ann 59:67–72
18. Oliaei SNB, Karpat Y (2014) Experimental investigations on micro milling of Stavax stainless steel. Procedia CIRP 14:377–382
19. Vilhena LM, Sedlacˇek M, Podgornik B, Vizˇintin J, Babnik A, Mozˇina J (2009) Surface texturing by pulsed Nd: YAG laser. Tribol Int 42:1496–1504
20. Etsion I (2005) State of the art in laser surface texturing. J Tribol 127:248–253
21. Li HN, Axinte D (2016) Textured grinding wheels: a review. Int J Mach Tools Manuf 109:8–35
22. Brinksmeier E, Mutlugünes Y, Klocke F, Aurich JC, Shore P, Ohmori H (2010) Ultra-precision grinding. CIRP Ann Manuf Technol 59:652–671
23. Aurich JC, Engmann J, Schueler GM, Haberland R (2009) Micro grinding tool for manufacture of complex structures in brittle materials. CIRP Ann Manuf Technol 58:311–314
24. Xie J, Zhuo YW, Tan TW (2011) Experimental study on fabrication and evaluation of micro pyramid-structured silicon surface using a V-tip of diamond grinding wheel. Precis Eng 35:173–182
25. Yutaka K, Hitoshi O, Hiroshi K, Teruko K (2015) Fabrication of micro-textured and plateau-processed functional surface by angled fine particle peening followed by precision grinding. CIRP Ann Manuf Technol 64:549–552
26. Bottene AC, Atoatte A, Silva EJ, Oliveira JFG, Marcos GP (2015) Blucher engineering proceedings. SIMEA 59(1):361–364
27. Stepien P (1989) Generation of regular patterns on ground surfaces. CIRP Ann 38(1):561–566
28. Stepien P (2007) Grinding forces in regular surface texture generation. Int J Mach Tool Manu 47:2098–2110
29. Stepien P (2007) Undeformed chip sizes in grinding process of regular surface texture generation. Arch Mech Eng 3:236–258
30. Stepien P (2011) Deterministic and stochastic components of regular surface texture generated by a special grinding process. Wear 271:514–518
31. da Silva EJ, de Oliveira JFG, Salles BB, Cardoso RS, Reis VRA (2013) Strategies for production of parts textured by grinding using patterned wheels. CIRP Ann 62:355–358
32. Oliveira JFG, Bottene AC, Franca TV (2010) A novel dressing technique for texturing of ground surfaces. CIRP Ann 59:361–364
33. da Silva EJ, Bottene AC, de Oliveira JFG, Atoatte A, de Souza Rodrigues A (2016) Grinding process for profiled texturing. CIRP Ann 65:337–340
34. Denkena B, de Leon L, Wang B (2009) Grinding of microstructured functional surfaces: a novel strategy for dressing of microprofiles. Production Engineering - Research and Development 3:41–48
35. Vollertsen F, Hu Z, Schulze Niehoff H, Theiler C (2004) State of the art in micro forming and investigations into micro deep drawing. J Mater Process Technol 151:70–79
36. Braun D, Greiner C, Schneider J, Gumbsch P (2014) Efficiency of laser surface texturing in the reduction of friction under mixed lubrication. Tribol Int 77:142–147
37. Chen X, Rowe WB (1996) Analysis and simulation of the grinding process. Part I: generation of the grinding wheel surface. Int J Mach Tools Manuf 36(8):871–882
38. Zhang C, Shin YC (2003) Wear of diamond dresser in laser assisted truing and dressing of vitrified CBN wheels. Int J Mach Tool Manuf 43:41–49
39. Chen X, Rowe WB (1996) Analysis and simulation of the grinding process—part II, mechanics of grinding. Int J Mach Tool Manu 36(8):883–896
40. Chen X, Rowe WB, Mills B, Allanson DR (1996) Analysis and simulation of the grinding process—part III, comparison with experiment. Int J Mach Tool Manu 36(8):897–906
41. Chen X, Rowe WB, Mills B, Allanson DR (1998) Analysis and simulation of the grinding process—part IV, effects of wheel wear. Int J Mach Tool Manu 38(1–2):41–49
42. Malkin S, Guo C (2008) Grinding technology: theory and application of machining with abrasives. Industrial Press, New York
43. Opoz T, Chen X (2012) Experimental investigation of material removal mechanism in single grit grinding. Int J Mach Tools Manuf 63:32–40